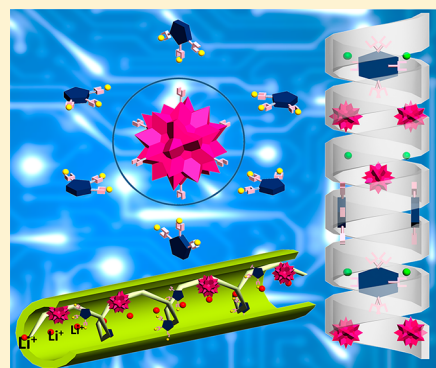# Assembly of Multifold Helical Polyoxometalate-Based Metal–Organic Frameworks as Anode Materials in Lithium-Ion Batteries

Meng-Ting Li,[†] Xi-Ya Yang,[†] Ji-Sen Li,[†] Ning Sheng,[†] Guo-Dong Liu,[†] Jing-Quan Sha,*[,†] and Ya-Qian Lan*[,‡]

[†]Key Laboratory of Inorganic Chemistry in Universities of Shandong, Department of Chemistry and Chemical Engineering, Jining University, Shandong 273155, China

[‡]Jiangsu Key Laboratory of Biofunctional Materials, School of Chemistry and Materials Science, Nanjing Normal University, Nanjing 210023, China

S *Supporting Information*

ABSTRACT: For exploring the multifold helical fabrication of polyoxometalate (POM)-based hybrid compounds, four POM-based crystalline compounds with different meso-helices, $H_3[Ag_{27}(trz)_{16}(H_2O)_6][SiW_{12}O_{40}]_2\cdot5H_2O$ (**1**), $H[Ag_{27}(trz)_{16}(H_2O)_4][PW_{12}O_{40}]_2\cdot2H_2O$ (**2**), $[Ag_{23}(trz)_{14}(H_2O)_2][HSiW_{12}O_{40}]$ (**3**), and $[Ag_{23}(trz)_{14}(H_2O)_2][PW_{12}O_{40}]$ (**4**), were successfully isolated by using the delicate 1,2,3-triazole ligand and silver ions in this work. Crystal analysis reveals that compounds **1** and **2** and compounds **3** and **4** are isomorphous and display 2-/4-fold mixed meso-helices and simple 2-fold meso-helices, respectively. In addition, due to the reversible multielectron redox behavior and electron storage functions of POMs, compounds **1** and **3** were studied as anode materials in lithium-ion batteries (LIBs). Compounds **1** and **3** show very high lithiation capacities (1356 and 1140 mAh g^{-1}, respectively) in the initial cycle, which are much higher than those of $(NBu_4)_4[SiW_{12}O_{40}]$ and commercial graphite at the current density of 100 mA g^{-1}. More importantly, both compounds also show good stable performance after 100 cycles.

INTRODUCTION

As a very significant geometric motif, helicity, a foundation of genetic codes in biological systems, has attracted great interest in its intriguing structures.[1−4] Inspired by sophisticated biological helices, chemists have been challenged to develop artificial helical polymers not only to mimic biological helices and functions but also for their potential applications in advanced materials, such as nonlinear optical devices,[5] the separation of enantiomers,[6] and asymmetric catalysis.[7] Thanks to the work of chemists, many novel artificial helical compounds have been rationally designed and synthesized to date,[8−12] but the design and syntheses of complex helical hybrid compounds are scarce.

Polyoxometalates (POMs), as a class of structurally well-defined inorganic building blocks, have exhibited a rich structural versatility and excellent physical and chemical properties in reported POM-based hybrid compounds,[13−16] among which POM-based metal−organic frameworks (POMOFs) have been widely explored because of their functional integrated and synergic effects. More importantly, POMs in the POMOFs may alter the equilibrium between metal ions and organic molecules.[17] In addition, taking into account the importance of helicity, the assembly of POMOFs with helical features may provide new possibilities in the pursuit of multifunctional materials with designed functional properties and aesthetic topological structures. In fact, POMs as versatile
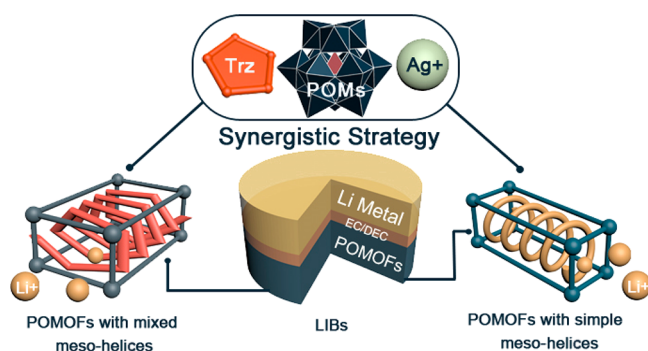
inorganic ligands have been shown to dominate and fabricate many helical POMOF compounds, such as the chiral triflexural helix dominated by $[HP_2Mo_5O_{23}]^{5-}$ clusters,[18] the interconnected and interweaved double helices by the $[Mo_8O_{26}]^{4-}$ polyoxoanion,[19] and POM-hanged double helices by the Keggin-type $[PMo_{12}O_{40}]^{3-}$ polyoxoanion.[20] Obviously these helical formations possess almost simple patterns, so the assembly of the mixed/complicated helical unit into a system is ardently expected, for as Nobel Laureate Jean-Marie Lehn pointed out, the evolution of the chemistry is toward more and more complex states and novel features.[21,22]

Currently, rechargeable Li-ion batteries (LIBs) have been dominating the market of portable electronic devices,[23,24] and graphite anodes are utilized in most commercial LIBs. However, they cannot meet the ever-increasing needs of power battery applications because of a limited theoretical capacity (ca. 372 mAh g^{-1}).[25] Inspiringly, POMs have been considered as electron reservoirs or sponges, arising from their multi-electron-transfer properties, which make them ideal candidates for electrode materials in LIBs.[26−30] Awaga and co-workers reported the pioneering work of using Keggin-type phosphomolybdate as the electrode to obtain a capacity of up to 320 Ah kg^{-1},[31] and then they further made an important

advance in theoretical and practical aspects for the use of Keggin $[PMo_{12}O_{40}]^{3-}$ as a cathode for LIBs.[32] Song and co-workers reported the tethered POM—pyrene hybridized with carbon nanotubes as an anode material to exhibit a capacity of 580 mAh g^{-1} for up to 100 cycles.[33] As the important branch of POM chemistry, the electrochemical performance study of POMOF materials is stirring because it can combine the advantages of POMs and MOFs together. A case in point is that POMOFs with novel structures as anode materials in LIBs, such as diamondoid, metallapillararene/metallacalixarene, cantane, and carbene structures, exhibit a higher reversible capacity as reported in our previous work (Table S1 in the Supporting Information).[34−36] Bearing these thoughts in mind, we aim to assemble POMOFs with helicity by using Keggin POMs, Ag ions, and 1,2,3-triazole ligands (trz) based on the following considerations: (I) Keggin POMs possess T_d symmetry and 36 potential oxygen atoms, which ensure fertile covalent coordination and flexible steric orientations (0−180°). (II) Three electron-donating trz molecules possess a small steric hindrance and flexible coordination mode, which favor the construction of multiple helices. (III) Soft d^{10} silver ions can adopt versatile coordination numbers (two to seven) and argentophilic interactions, which enhance the opportunity to coordinate with the POMs. Moreover, Ag is the best electronic conductor. As a result, a series of POMOFs with different multifold meso-helices, $H_3[Ag_{27}(trz)_{16}(H_2O)_6][SiW_{12}O_{40}]_2\cdot5H_2O$ (1), $H[Ag_{27}(trz)_{16}(H_2O)_4][PW_{12}O_{40}]_2\cdot2H_2O$ (2), H-$[Ag_{23}(trz)_{14}(H_2O)_2][SiW_{12}O_{40}]$ (3), and $[Ag_{23}(trz)_{14}(H_2O)_2]$-$[PW_{12}O_{40}]$ (4), were isolated under different pH values in this work. Structural analysis shows that compounds 1 and 2 contain 2-/4-fold mixed meso-helices and compounds 3 and 4 contain single 2-fold helices (Scheme 1). With the voltage window of 0.01−3 V, compounds 1 and 3 as anode materials for LIBs show gratifying discharge capacities of 456 and 360 mAh g^{-1} at 100 mA g^{-1} after 100 cycles.

Scheme 1. Representations of the Assembly of Keggin POMs, Ag Ions, and trz Ligands Based on a Synergistic Strategy and POMOFs with Different Helices as Anode Materials, Li as the Counter Electrode, and EC/DEC (1:1 v/v) as the Electrolyte in Lithium-Ion Batteries (LIBs)

EXPERIMENTAL SECTION

Materials and Methods. All reagents were purchased commercially and used without further purification. Elemental analyses for C, H, and N were performed on a PerkinElmer 2400 CHN Elemental Analyzer. The IR spectrum was obtained on an Alpha Centaurt FT/IR spectrometer with a KBr pellet in the 400−4000 cm^{-1} region. The XRPD patterns were obtained with a Rigaku D/max 2500V PC diffractometer with Cu Kα radiation; the scanning rate was 4° s^{-1}, with

2θ ranging from 5° to 40°. XPS analyses were performed on a thermo ESCALAB 250 spectrometer with a Mg Kα achromatic X-ray source. The thermogravimetric analyses (TGA) were carried out on a PerkinElmer-7 thermal analyzer at a heating rate of 10 °C min^{-1}.

Synthesis of $H_3[Ag_{27}(trz)_{16}(H_2O)_6][SiW_7^{VI}W_5^VO_{40}]_2\cdot5H_2O$ (1). The mixture of $H_4SiW_{12}O_{40}$ (300 mg, 0.10 mmol), AgNO$_3$ (150 mg, 0.89 mmol), trz (30 mg, 0.43 mmol), and NH$_4$VO$_3$ (36 mg, 0.3 mmol) was dissolved in distilled water (10 mL) while being stirred for 0.5 h at room temperature, and the pH value was adjusted to ca. 1.5 by 1 mol L^{-1} HCl. The resulting solution was transferred into a 20 mL Teflon-lined stainless steel container and heated at 170 °C for 3 days. After the autoclave was cooled to room temperature at 10 °C h^{-1}, the dark-red block crystals suitable for X-ray crystallography were obtained, washed with distilled water, and air-dried (yield: 45% based on Ag). Elemental analysis anal. calcd for 1 ($C_{32}H_{57}Ag_{27}N_{48}O_{91}Si_2W_{24}$ (9951.08)): C 3.86, H 0.58, N 6.75%; found C 3.82, H 0.69, N 6.71%. IR spectra (Figure S8): characteristic bands at 1183, 905, and 774 cm^{-1} are attributed to ν(Si—O), ν(W=O), and ν(W—O—W) vibrations, respectively; bands in the regions of 1600−1250 cm^{-1} are attributed to the trz ligand. Compound 1 is also stable in the acidic pH range of 1−12 and basic aqueous electrolyte solutions at room temperature, as confirmed by subsequent FT/IR measurements (Figures S13 and S15).

Synthesis of $H[Ag_{27}(trz)_{16}(H_2O)_4][PW_7^{VI}W_5^VO_{40}]_2\cdot2H_2O$ (2). Compound 2 was prepared in a manner similar to that described for compound 1, except that $H_4SiW_{12}O_{40}$ (300 mg, 0.10 mmol) replaced $H_3PW_{12}O_{40}$. Dark-red block crystals were obtained (yield: 38% based on Ag). Elemental analysis anal. calcd for 2 ($C_{32}H_{45}Ag_{27}N_{48}O_{86}P_2W_{24}$ (9864.76)): C 3.90, H 0.46, N 6.82%; found C 3.87, H 0.71, N 6.79%. IR spectra (Figure S8): characteristic bands at 1074, 954, and 791 cm^{-1} are attributed to ν(P—O), ν(W=O), and ν(W—O—W) vibrations, respectively; bands in the regions of 1600−1250 cm^{-1} are attributed to the trz ligand.

Synthesis of $[Ag_{23}(trz)_{14}(H_2O)_2][HSiW_6^{VI}W_6^VO_{40}]$ (3). The synthesis process of 3 is similar to that of 1, except that the pH value of the mixture was adjusted to 2.5 by 1 mol L^{-1} HCl. Dark-yellow block crystals were obtained (yield: 36% based on Ag). Elemental analysis anal. calcd for 3 ($C_{28}H_{33}Ag_{23}N_{42}O_{42}SiW_{12}$ (6345.08)): C 5.30, H 0.52, N 9.27%; found C 5.32, H 0.61, N 9.35%. IR spectra (Figure S8): characteristic bands at 1194, 909, and 773 cm^{-1} are attributed to ν(Mo=O), ν(Si—O), and ν(Mo—O—Mo) vibrations, respectively; bands in the regions of 1600−1250 cm^{-1} are attributed to the trz ligand. Compound 3 is also stable in the acidic pH range of 1−12 and basic aqueous electrolyte solutions at room temperature, as confirmed by subsequent FT/IR measurements (Figures S13 and S15).

Synthesis of $[Ag_{23}(trz)_{14}(H_2O)_2][PW_6^{VI}W_6^VO_{40}]$ (4). Compound 4 was prepared in a manner similar to that described for 3, except that $H_4SiW_{12}O_{40}$ (300 mg, 0.10 mmol) replaced $H_3PW_{12}O_{40}$. Dark-yellow crystals were obtained (yield: 37% based on Ag). Elemental analysis anal. calcd for 3 ($C_{28}H_{32}Ag_{23}N_{42}O_{42}PW_{12}$ (6346.96)): C 5.30, H 0.51, N 9.27%; found C 5.34, H 0.64, N 9.34%. IR spectra (Figure S8): characteristic bands at 1067, 954, and 787 cm^{-1} are attributed to ν(P—O), ν(W=O), and ν(W—O—W) vibrations, respectively; bands in the regions of 1600−1250 cm^{-1} are attributed to the trz ligand.

Battery Analyses. The crystal water molecules in compounds 1 and 3 were removed at 100 °C in a vacuum oven before they were used as electrode materials. The as-prepared compounds 1 and 3 and $(NBu_4)_4[SiW_{12}O_{40}]$ were used as the anode materials to study the electrochemical performance of LIBs. For each sample, super-P carbon and polyvinylidene fluoride (PVDF) binders were mixed together, and an N-methyl-2-pyrrolidinone (NMP) solvent was added to the mixture to form a slurry with an appropriate viscosity. The final mixture consisted of 70% title compound, 20% super-P carbon, and 10% PVDF binder. The slurry was deposited onto copper foils and dried under a vacuum at 60 °C for 24 h. The loading mass of electroactive materials in the electrode slurry was ~2 mg cm^{-2}. The testing coin cells were assembled in an argon-filled glovebox (oxygen and water concentration maintained below 1 ppm) with the working electrode as

Table 1. Crystal Data for the Compounds 1−4

chemical formula	$C_{32}H_{57}Ag_{27}N_{48}O_{91}Si_2W_{24}$	$C_{32}H_{45}Ag_{27}N_{48}O_{86}P_2W_{24}$	$C_{28}H_{33}Ag_{23}N_{42}O_{42}SiW_{12}$	$C_{28}H_{32}Ag_{23}N_{42}O_{42}PW_{12}$
formula weight	9951.08	9756.67	6345.08	6346.96
temperature (K)	296	293	296	298
wavelength (Å)	0.71073	0.71073	0.71073	0.71073
crystal system	triclinic	triclinic	monoclinic	monoclinic
space group	$P\bar{1}$	$P\bar{1}$	$C2/c$	$C2/c$
a (Å)	14.59	14.75	19.68	19.65
b (Å)	15.27	15.35	22.14	22.11
c (Å)	17.96	16.78	23.15	23.14
α (deg)	89.12	87.26	90	90
β (deg)	85.54	85.77	100.85	100.98
γ (deg)	63.87	65.73	90	90
V (Å^3)/Z	3580.6/1	3451.96/1	9904.1/4	9873.3/4
density (g cm^{-3})	4.588	4.724	4.233	4.248
abs. coeff. (mm^{-1})	22.611	23.755	22.480	22.617
$F(000)$	4329	4329	10362	10428
data collection θ range	1.49−25.00	3.337−25.000	1.55−25.00	3.46−25.00
reflns collected	27550	24863	24653	88908
independent reflns	12496	12148	8744	8693
R_{int}	0.0453	0.0629	0.0383	0.0467
data/restraints/parameters	12496/120/1012	12148/208/981	8744/114/701	8693/108/696
final R indices $[I > 2\delta(I)]^a$	$R_1 = 0.0756$, $wR_2 = 0.2164$	$R_1 = 0.0698$, $wR_2 = 0.1947$	$R_1 = 0.0676$, $wR_2 = 0\ 0.145$	$R_1 = 0.0511$, $wR_2 = 0.1525$
largest diff. peak and hole (e Å^{-3})	4.479 and −4.743	4.636 and −3.660	3.538 and −2.446	5.764 and −3.324

$^aR_1 = \sum(||F_0| - |F_c||)/\sum|F_0|$ and $wR_2 = \sum[w(|F_0|^2 - |F_c|^2)^2]/\sum[w(|F_0|^2)^2]^{1/2}$.

fabricated, metallic lithium foil as the counter electrode, and 1.0 M LiPF$_6$ in ethylene carbonate/diethyl carbonate (1:1 v/v) as the electrolyte. Galvanostatic charge/discharge cycles were performed on a LAND 2001A instrument (Wuhan, China) and electrochemical workstation (Princeton Applied Research, Germany) to record the circulation measurements and to perform cyclic voltammetry (CV) and electrochemical impedance spectroscopy (EIS) of the batteries at a constant ambient temperature. The specific capacity was calculated based on the mass of active material.

X-ray Crystallographic Study. Crystallographic data for compounds **1**−**4** were collected on a Bruker SMART-CCD diffractometer with Mo Kα radiation ($\lambda = 0.71073$ Å). The structures were solved by the direct method and refined via full-matrix least squares on F^2 through the SHELXTL and WINGX software packages.[37] All non-hydrogen atoms were refined anisotropically, and the "ISOR" command was used to refine some ADP problems. Crystal data and structure refinement for compounds **1**−**4** are listed in Table 1. Supplementary crystallographic data can be found via CCDC numbers 1813090−1813093 for compounds **1**−**4**, respectively. Selected bond lengths and angles of **1**−**4** are listed in Tables S2−S5, respectively, in the Supporting Information.

■ RESULTS AND DISCUSSION

Analysis of Structure. Single-crystal X-ray diffraction analyses reveal that compounds **1** and **2** and compounds **3** and **4** are isomorphous, where the unit cell dimensions, volumes, and related bond distances and angles are only slightly different. Thus, the structures of **1** and **3** were discussed in detail as typical representatives. Compound **1** crystallizes in the triclinic space group $P\bar{1}$ and consists of one $[SiW_{12}O_{40}]^{4-}$ polyanion (abbreviated to SiW$_{12}$), 14 Ag$^+$ ions (the position of one Ag$^+$ ion has half-site occupancy), and eight 1,2,3-triazole ligands (abbreviated to trz) (Figure S1). The oxidation states of W atoms are confirmed by XPS measurements. The crystallographic unit of **3** crystallizes in the monoclinic space group $C2/c$ and contains one-half of a SiW$_{12}$ polyanion, 12 Ag$^+$ ions, and seven trz ligands (Figure S1). The central SiO$_4$ tetrahedron in **3** is disordered with a half-occupation of O atoms. This kind of

disorder often appears in the Keggin clusters, which was explained by Evans and Pope[38] who said that the disorder was a crystallographic result, namely, a single Keggin anion was self-superimposed by a second one by rotating 90° about a C4 axis.

In **1**, Ag1 and Ag10 ions adopt a tetradentate coordination mode, and Ag2, Ag5, Ag7, and Ag14 ions adopt a bidentate coordination mode; meanwhile, Ag3, Ag4, Ag8, Ag9, and Ag11−Ag13 exhibit a "T-shaped" geometric coordination. The bond lengths around Ag$^+$ ions are in the normal range of 2.047−2.313 Å for Ag−N bonds and 2.319−2.828 Å for Ag−O bonds. Without regard to the SiW$_{12}$ polyanions, two similar organic−metal subunit motifs could be identified: Type-I and Type-II subunits (Figure 1a and 1c), which consist of four trz ligands and five Ag$^+$ ions and have different Ag$^+$ centers (Ag10 for I and Ag2 for II). In turn, each SiW$_{12}$ polyanion connects with 13 Ag$^+$ ions (Figure 1b), assembling into the one-dimensional POM−Ag chain (Figure S2).

An interesting structure is formed when Type-I subunits and SiW$_{12}$ polyanions construct the 2-fold meso-helices along the a axis as shown in Figure 1d, in which the left- and right-handed helices are fabricated along the same route of [SiW$_{12}$-subunit I-SiW$_{12}$-subunit I-SiW$_{12}$]$_n$. Then, the left- and right-handed helical chains are connected together by sharing SiW$_{12}$ polyanions, forming one-dimensional double helical tunnels. Further, the adjacent tunnels connect with each other by sharing Type-I subunits to form the 2-fold meso-helices array (Figure S3a), in which the Type-I subunits act as the universal vertices. Note that another kind of helix with 4-fold helicity is constructed by the Type-II subunits and SiW$_{12}$ polyanions along the a axis as shown in Figure 1e, namely, each helix is fabricated in the same way along the route of [SiW$_{12}$−Type-II−SiW$_{12}$−Type-II−SiW$_{12}$]$_n$ with an identical thread pitch of 29.372 Å, which is two times as long as the 2-fold meso-helices. Moreover, the 4-fold helices are enclosed in a smaller tunnel by sharing themselves. Finally, adjacent 4-fold helical tunnels are connected to each other to form a 4-fold meso-helices array
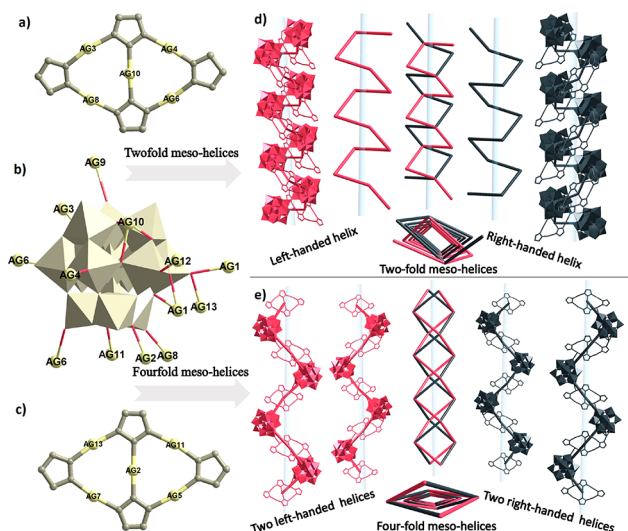
Figure 1. (a) Representation of Type-I subunits with a Ag10 center. (b) The coordination pattern of the SiW$_{12}$ polyanion. (c) The Type-II subunit with a Ag2 center. (d) View of 2-fold meso-helices constructed by Type-I subunits and SiW$_{12}$ polyanions. (e) View of 4-fold meso-helices constructed by Type-II subunits and SiW$_{12}$ polyanions in compound **1**.
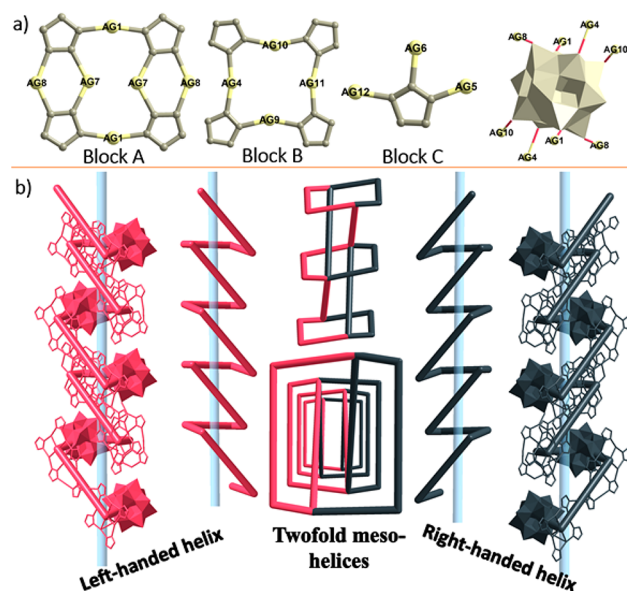

Figure 2. (a) Ball/stick/polyhedral representations of the three building blocks and the coordination pattern of the SiW$_{12}$ polyanion of compound **3**. (b) Ball/stick/polyhedral representations of the left- and right-handed helical chains.

along the *b* axis (Figure S3b). From an overall perspective, the alternating connections between 4-fold meso-helices arrays and 2-fold meso-helices arrays generate together the whole three-dimensional framework using SiW$_{12}$ polyanions as their common vertices (Figure S4). Ultimately, we use a topology analysis to simplify the complex structures of compound **1**. More specifically, the Type-I subunits act as 5-connected nodes, Type-II subunits as 6-connected nodes, and SiW$_{12}$ polyanions as 10-connected nodes. The whole framework can be simplified as a 5,6,10-net with the point symbol of $\{3\cdot4^{22}\cdot5^{7}\cdot6^{15}\}$ $\{3^{2}\cdot4^{10}\cdot5^{3}\}$ $\{4^{10}\}$.

In **3**, Ag5 and Ag11 ions adopt a bidentate coordination mode and the Ag2 ion exhibits a "V-shaped" geometric coordination. Ag1, Ag4, Ag6, Ag9, and Ag12 ions adopt a distorted T-shaped geometric coordination, whereas Ag8 exhibits a "Y-shaped" geometric coordination. Ag3, Ag7, and Ag10 ions exhibit a tetradentate tetrahedral coordination geometry. The bond lengths around the Ag^{+} ions are in the normal range of 2.056−2.264 Å for Ag−N bonds, 2.403−2.870 Å for Ag−O bonds, and 2.667−2.801 Å for Ag−Ag bonds (the sum of the van der Waals radii of Ag and O is 3.20 Å[39]). The cationic host framework is composed of three basic building blocks, namely, the [Ag$_{6}$(trz)$_{4}$] closed ring (block A), the [Ag$_{4}$(trz)$_{4}$] extensible ring (block B), and trident [Ag3(trz)] (block C), as shown in Figure 2a. More specifically, four trz ligands connect with four Ag^{+} ions to form a [Ag$_{6}$(trz)$_{4}$]$^{2+}$ cation ring (block A), in which all the N atoms of the trz ligand are used. In block B, four Ag ions were linked by four trz ligands to give rise to an extensible ring, and the trz ligand adopts a pyrazole-like coordination mode. Block C is constructed by a trident trz molecule linked by three Ag ions. When trz ligands are not taken into account, SiW$_{12}$ polyanions connect with eight Ag^{+}, forming an isolated POM−Ag cluster. The interesting part is that the 2-fold helical pattern is found along the *c* axis, as shown in Figure 2b. The left and right helix adopt the same route of [block B-SiW$_{12}$-block A-block B-block C-block B-block A-SiW$_{12}$-block B]$_n$ with an identical thread pitch of 23.15 Å. Note that the argentophilic Ag−Ag

interactions play important roles between block A and block B. Moreover, the left and right helix are enclosed in a square tunnel by sharing block B (Figure S5). Finally, four adjacent tunnels are connected to each other via sharing one side of the tunnel, where the SiW$_{12}$ polyanions and block B support the framework (Figures S6 and S7). Via application of a topological analysis to simplify the structure of **3**, block C acts as 2-connected nodes, block B acts as 5-connected nodes, block A acts as 6-connected nodes, and SiW$_{12}$ polyanions act as 8-connected nodes. Then, the whole framework can be simplified as a 2,5,6,10-net with the point symbol of $\{3\cdot4\cdot5\cdot6^{4}\cdot7^{2}\cdot8\}^{2}\{3^{2}\cdot4^{4}\cdot5^{4}\cdot6^{4}\cdot7\}$ $\{3^{2}\cdot4^{6}\cdot5^{6}\cdot6^{8}\cdot7^{4}\cdot8\cdot9\}\{6\}^{2}$.

By the utilization of the same ingredients, two kinds of different helical configurations have been fabricated and summarized, as shown in Figure 3. We speculate that the excellent nature of Keggin POMs and the three electron-donating trz ligands dominates the evolution of the helical architectures. It is known that the construction of POMOFs mainly depends on the coordination nature of the metal ions/POMs, the steric hindrance of the ligands, and their geometrical relations. On the positive side, the small and delicate trz ligands can provide an excellent transportation system for Ag^{+} ions to connect with the POM polyanions. On the other hand, Keggin POMs as transferable building blocks with multiple twisted V-shaped coordination modes contribute to the construction of the helical configuration, namely, the higher the coordination number of the POM polyanions, the more successful the chance of constructing a helical configuration. When compounds **1** with **3** are compared, compound **1** is isolated under a relatively lower pH, in which Ag^{+} ions are not inclined to hydrolyze so there exist sufficient Ag^{+} ions for the coordination with POM polyanions. With the pH value continuously increasing, free Ag^{+} ions decrease greatly for **3**, such that the POM polyanions decrease the opportunities for combinations with Ag^{+} ions. As a result, the coordination number of POM polyanions in **1** is higher than that of **3**, and
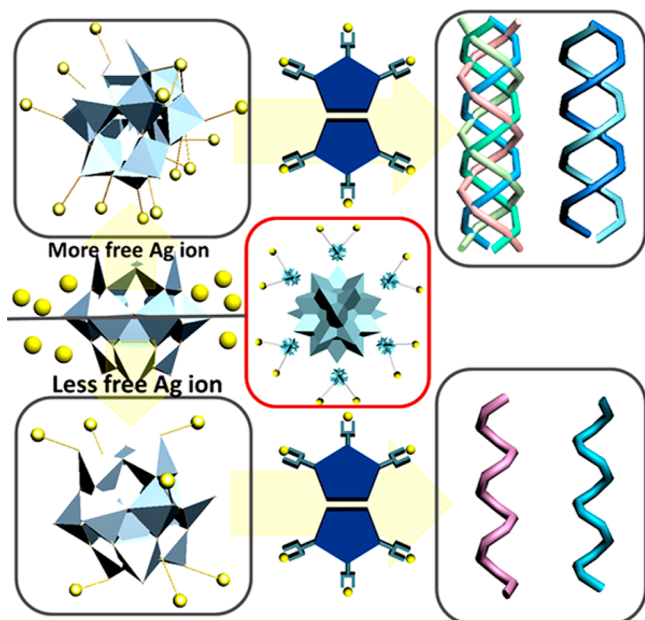
Figure 3. Schematic representation of the strategy for synthesis of two different helical patterns.

Figure 4. Cyclic voltammograms of compounds **1** (a) and **3** (b) as anode materials in the range of 0.01−3 V.

compound **1** exhibits a more complex helical configuration compared with that of **3**.

XPS, PXRD, and TG Analyses. The oxidation states of W atoms in compounds **1**−**4** are confirmed by XPS measurements (Figures S9 and S10). The XPS measurement shows four partially overlapped peaks, and the fit of the curve gives the positions of these four peaks at about 34.9, 35.3, 37.1, and 37.5 eV being attributed to $W^V4f_{7/2}$, $W^{VI}4f_{7/2}$, $W^V4f_{5/2}$, and $W^{VI}4f_{5/2}$, respectively. The results are consistent with the structural analyses and charge balance, indicating that the W^{VI} was partially reduced to W^V in the synthetic procedure. The XRD patterns for compounds **1**−**4** are presented in Figure S11. The diffraction peaks of both simulated and experimental patterns match well, except for a little difference in reflection intensities, thus indicating that the new compounds are in the purity phase. The thermal stability curves are shown in Figure S12. For compound **1**, the thermal analysis exhibits two steps of weight loss: the first loss is 1.93% at about 40−250 °C, corresponding to the loss of all water (calcd 1.98%), and the second loss is 13.09% (calcd 13.11%) at 280−500 °C, arising from the decomposition of trz organic molecules. For compound **2**, the thermal analysis exhibits two steps of weight loss: the first loss is 1.10% at about 40−250 °C, corresponding to the loss of all water (calc. 1.11%), and the second loss is 12.43% (calc. 12.46%) at 280−500 °C, arising from the decomposition of trz organic molecules. For compounds **3** and **4**, the thermal analysis shows similar steps of weight loss; more specifically, the first weight loss is 0.58% (calc. 0.57%) for **3** and 0.57% (calc. 0.57%) for **4**, corresponding to the decomposition of the water molecules. The total weight loss is 15.82% (calc. 15.80%) for **3** and 15.82% (calc. 15.80%) for **4**, which corresponds to the decomposition of trz organic molecules.

Electrochemical Performance. To investigate the potential application of the helical POMOFs, compounds **1** and **3** were used as electrode materials and incorporated into coin-type half-cells. The cyclic voltammetry (CV) curves of compounds **1** and **3** at a scan rate of 0.1 mV s^{-1} in the voltage range of 0.01−3.0 V are shown in Figure 4. An
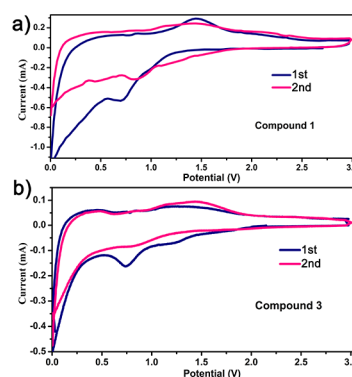
irreversible reduction peak at 0.7 V could be observed only in the first cycle for both compounds **1** and **3**, indicating the formation of a solid electrolyte interphase,[40,41] which disappears in the following cycles. In addition, the reduction signal between 0.01 and 0.2 V can be attributed to the Li$^+$ insertion reaction.[42]

To understand the influence of helicity on battery performance, the insoluble $(NBu_4)_4[SiW_{12}O_{40}]$ as an anode material was also explored. The charge−discharge voltage profiles of the **1**, **3**, and $(NBu_4)_4[SiW_{12}O_{40}]$ electrodes with a current density of 100 mA g^{-1} for the first two cycles and the 50th cycles are shown in Figure 5. The first discharge capacities of the **1** and **3**
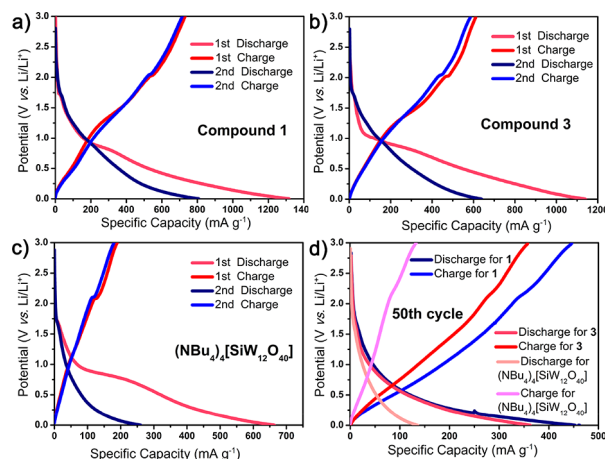

Figure 5. Galvanostatic charge−discharge curves of (a) **1**, (b) **3**, and (c) $(NBu_4)_4[SiW_{12}O_{40}]$ anodes during the initial two cycles and (d) galvanostatic charge−discharge curves at the 50th cycle at a current density of 100 mA g^{-1}.

anodes are 1356 and 1140 mAh g^{-1}, respectively, while the first discharge capacity of $(NBu_4)_4[SiW_{12}O_{40}]$ is only 663 mAh g^{-1}, all of which are still much better than that of commercial graphite.[38] The capacities are reduced to 832 mAh g^{-1} for **1**, 639 mAh g^{-1} for **3**, and 139 mAh g^{-1} for $(NBu_4)_4[SiW_{12}O_{40}]$ in the second cycle. The significant loss of capacity during the initial cycles is attributed to the formation of SEI films, a common phenomenon in LIBs. After the initial drop, the capacity maintains a stable value at ca. 456 mAh g^{-1} for **1** and 360 mAh g^{-1} for **3** after 100 cycles. It is worth noting that the Coulombic efficiencies can all reach a plateau at ∼99% after 35 cycles, where they remain stable, which indicates their commendable cycling stabilities (Figure 6). In comparison,
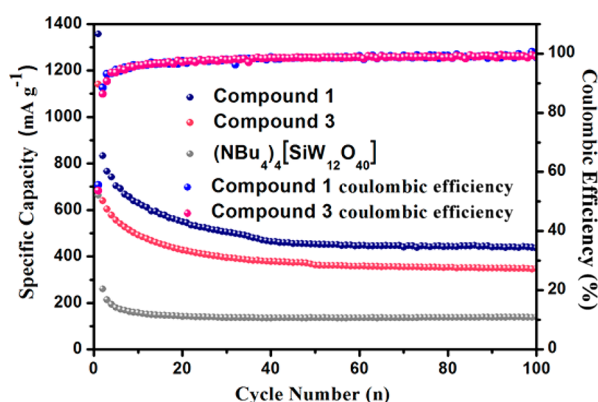
Figure 6. Discharge capacity and Coulombic efficiency of **1**, **3**, and $(NBu_4)_4[SiW_{12}O_{40}]$ anodes at a current density of 100 mA g^{-1}.

the capacity of the $(NBu_4)_4[SiW_{12}O_{40}]$ anode changes to ca. 139 mAh g^{-1} after 100 cycles at the same current density. It is obvious that the discharge capacities of **1** and **3** as anode materials for LIBs have greater advantages over their corresponding matrix, which might be attributed to the orderly helical structure (providing a suitable and stable Li$^+$ ion and/or electron transmission pathway) and POMs as stable electron donors.

The rate performance and cycling stability during lithium-ion insertion−extraction processes are key factors for practical applications. Hence, the rate capabilities of compounds **1** and **3** have been evaluated at various current densities of 100, 200, 500, and 1000 mA g^{-1} at the cutoff voltage between 0.01 and 3.0 V vs Li$^+$/Li, respectively, giving discharge specific capacities of ca. 600, 490, 350, and 248 mAh g^{-1} for **1** and 510, 390, 249, and 170 mAh g^{-1} for **3** (Figure 7a). When the current density
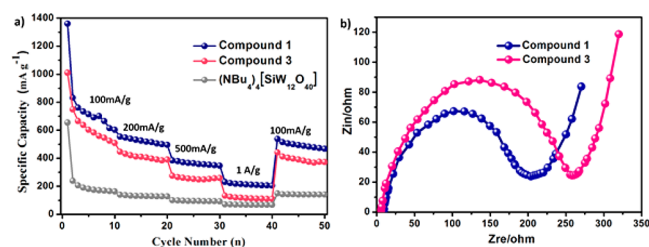

Figure 7. (a) Rate performance of **1**, **3**, and $(NBu_4)_4[SiW_{12}O_{40}]$ anodes at current densities between 100 mA g^{-1} and 1 A g^{-1}. (b) Nyquist plots of the **1** and **3** anodes after the first discharge−charge process. Insert: the simulated equivalent circuit of the electrode/electrolyte interface.

resets to 100 mA g^{-1}, the capacity can be restored to the original specific capacities. The results verify the high stability of the compounds **1** and **3** as LIB anode materials. In contrast, the capacity of the $(NBu_4)_4[SiW_{12}O_{40}]$ anode is much lower than those of the other anodes at each current density. Moreover, the cycling and rate performance of commercial graphite as an anode for LIBs were studied in our previous work, and the reversible capacity at 100 mA g^{-1} is 320 mAh g^{-1}, after the initial drop, and remains at 200 mAh g^{-1} at 1 A g^{-1}. Therefore, compound **1** has a larger advantage than graphite. Electrochemical impedance spectroscopy (EIS) was used for evaluating the electrochemical behavior of the **1** and **3** anodes, and the equivalent circuit model is introduced into the analysis system. As shown in Figure 7b, R_e, R_f, and R_{ct} in the circuit

model represent the electrolyte resistance, SEI film resistance, and the charge-transfer resistance, respectively. The Warburg impedance (Z_w) represents the diffusion of Li$^+$ ions into the bulk electrode. Both CPE$_f$ and CPE$_{ct}$ represent the constant phase element. The values of R_e and R_{ct} are 9.3 and 192.7 Ω for **1** and 5.9 and 253.1 Ω for **3**, respectively, which indicates that the complex multifold meso-helices of compound **1** may support electron conductivities that are relatively better than those of compound **3**.

■ CONCLUSION

In this work, by employing a small and delicate 1,2,3-triazole ligand and soft d^{10} silver ions with versatile coordination numbers to modify the Keggin polyanion, four helical POM-based MOFs were successfully isolated and structurally characterized, which display 2-/4-fold mixed meso-helices for **1** and **2** and single 2-fold meso-helices for **3** and **4**. In the synthesis of helical POMOFs, POM polyanions with multiple twisted V-shaped coordination modes and the pH value of system play key roles for self-assembly helical patterns. When directly applied as the LIB anode materials, compounds **1** and **3** exhibit specific discharge capacities of 1356 and 1140 mAh g^{-1} at first cycle, respectively. Note that compound **1** exhibits a better cycle capacity and rate performance compared to those of compound **3**, which indicates that the complex helical conformations may provide a more stable charge transmission channel during the discharge−charge process. More should be done to construct more POMOFs with complex helical structures and superior electrochemical performance.

■ ASSOCIATED CONTENT

ⓢ Supporting Information
The Supporting Information is available free of charge on the ACS Publications website at DOI: 10.1021/acs.inorg-chem.7b03228.

> Tables of selected bond lengths and bond angles for compounds **1**−**4**; partial structural figures of compounds **1**−**4**; and IR, PXRD, XPS, and TGA analyses (PDF)

Accession Codes
CCDC 1813090−1813093 contain the supplementary crystallographic data for this paper. These data can be obtained free of charge via www.ccdc.cam.ac.uk/data_request/cif, or by emailing data_request@ccdc.cam.ac.uk, or by contacting The Cambridge Crystallographic Data Centre, 12 Union Road, Cambridge CB2 1EZ, UK; fax: +44 1223 336033.

■ AUTHOR INFORMATION

Corresponding Authors
*E-mail: shajq2002@126.com.
*E-mail: yqlan@njnu.edu.cn.

ORCID ⓘ
Xi-Ya Yang: 0000-0002-8632-1993
Ji-Sen Li: 0000-0003-2578-422X
Jing-Quan Sha: 0000-0002-5925-9565
Ya-Qian Lan: 0000-0002-2140-7980

Notes
The authors declare no competing financial interest.

■ REFERENCES

(1) Piguet, C.; Bernardinelli, G.; Hopfgartner, G. Helicates as versatile supramolecular complexes. *Chem. Rev.* **1997**, *97*, 2005−2062.

(2) Berl, V.; Huc, I.; Khoury, R. G.; Krische, M. J.; Lehn, J. M. Interconversion of single and double helices formed from synthetic molecular strands. *Nature* **2000**, *407*, 720−723.

(3) Piguet, C.; Borkovec, M.; Hamacek, J.; Zeckert, K. Strict self-assembly of polymetallic helicates: the concepts behind the semantics. *Coord. Chem. Rev.* **2005**, *249*, 705−726.

(4) Bu, X. H.; Tong, M. L.; Chang, H. C.; Kitagawa, S.; Batten, S. R. A Neutral 3D Copper Coordination Polymer Showing 1D Open Channels and the First Interpenetrating NbO−Type Network. *Angew. Chem., Int. Ed.* **2004**, *43*, 192−195.

(5) Botek, E.; Castet, F.; Champagne, B. Theoretical Investigation of the Second-Order Nonlinear Optical Properties of Helical Pyridine−Pyrimidine Oligomers. *Chem. - Eur. J.* **2006**, *12*, 8687−8695.

(6) Okamoto, Y. Helical Polymers for Efficient Enantiomer Separation. *Adv. Polym. Sci.* **2013**, *261*, 391−414.

(7) Wang, S.; Chen, J.; Feng, X.; Shi, G.; Zhang, J.; Wan, X. Conformation Shift Switches the Chiral Amplification of Helical Copoly (phenylacetylene) s from Abnormal to Normal "Sergeants-and-Soldiers" Effect. *Macromolecules* **2017**, *50*, 4610−4615.

(8) Soghomonian, V.; Chen, Q.; Haushalter, R. C.; Zubieta, J.; O'Connor, C. J. An inorganic double helix: hydrothermal synthesis, structure, and magnetism of chiral $(CH_3)_2NH_2K_4V_{10}O_{10}(H_{20})_2(OH)_4(PO_4)_7$ 4H$_2$O. *Science* **1993**, *259*, 1596−1600.

(9) Chen, X. M.; Liu, G. F. Double-stranded helices and molecular zippers assembled from single-stranded coordination polymers directed by supramolecular interactions. *Chem. - Eur. J.* **2002**, *8*, 4811−4817.

(10) Yashima, E.; Maeda, K.; Iida, H.; Furusho, Y.; Nagai, K. Helical polymers: synthesis, structures, and functions. *Chem. Rev.* **2009**, *109*, 6102−6211.

(11) Sun, Y.; An-Xin, W. Hydrogen-bonding induced construction of a multiple double-helical system via a macrocycle-containing propargylamine backbone. *Supramol. Chem.* **2015**, *27*, 420−424.

(12) Wei, Q.; Ding, Y. J.; Huang, X.; Zhang, J. Y.; Lu, W. J.; Dong, R. F.; Si, L. P.; Cai, Y.-P. Metal cation-dependent helicity of two 1-D heterometal chains constructed from pyridine-2, 6-dicarboxylate. *Inorg. Chem. Commun.* **2016**, *73*, 52−56.

(13) Qin, J. S.; Du, D. Y.; Guan, W.; Bo, X. J.; Li, Y. F.; Guo, L. P.; Zhou, H. C.; Su, Z.-M.; Wang, Y.-Y.; Lan, H.-C. Ultrastable polymolybdate-based metal−organic frameworks as highly active electrocatalysts for hydrogen generation from water. *J. Am. Chem. Soc.* **2015**, *137*, 7169−7177.

(14) Zhao, X.; Duan, Y.; Yang, F.; Wei, W.; Xu, Y.; Hu, C. Efficient Mechanochemical Synthesis of Polyoxometalate⊂ZIF Complexes as Reusable Catalysts for Highly Selective Oxidation. *Inorg. Chem.* **2017**, *56*, 14506−14512.

(15) Wang, X. L.; Li, N.; Tian, A. X.; Ying, J.; Li, T. J.; Lin, X. L.; Yang, Y.; Luan, J. Unprecedented application of flexible bis (pyridyl-tetrazole) ligands to construct helix/loop subunits to modify polyoxometalate anions. *Inorg. Chem.* **2014**, *53*, 7118−7129.

(16) Yang, X. Y.; Wei, T.; Li, J. S.; Sheng, N.; Zhu, P. P.; Sha, J. Q.; Lan, Y. Q.; Wang, T. Polyoxometalate-incorporated metallapillarar-ene/metallacalixarene metal-organic frameworks as anode materials for lithium ion batteries. *Inorg. Chem.* **2017**, *56*, 8311−8318.

(17) Xu, X.; Chen, S.; Chen, Y.; Sun, H.; Song, L.; He, W.; Wang, X. Polyoxometalate Cluster-Incorporated Meta-Organic Framework Hierarchical Nanotubes. *Small* **2016**, *12*, 2982−2990.

(18) Qin, C.; Wang, X. L.; Yuan, L.; Wang, E. B. Chiral self-threading frameworks based on polyoxometalate building blocks comprising unprecedented tri-flexure helix. *Cryst. Growth Des.* **2008**, *8*, 2093−2095.

(19) Sun, W.; Zhang, C.; Ma, H.; Pang, H.; Li, S. The coexistence of interconnected and interweaved double helices in an octamolybdate-based compound: synthesis, structure, and photocatalytic properties. *Dalton Trans.* **2014**, *43*, 16322−16327.

(20) Wang, X.; Zhang, H.; Wang, X.; Li, T.; Li, N.; Xu, N.; Liu, G.; Lin, H. A novel Keggin-type molybdophosphate-based helix metal-organic chain and its polypyrrole composite: Synthesis, structure and properties. *Inorg. Chem. Commun.* **2017**, *75*, 16−20.

(21) Lehn, J. M. Perspectives in chemistry—steps towards complex matter. *Angew. Chem., Int. Ed.* **2013**, *52*, 2836−2850.

(22) Lehn, J. M. Toward self-organization and complex matter. *Science* **2002**, *295*, 2400−2403.

(23) Tang, Y.; Zhang, Y.; Li, W.; Ma, B.; Chen, X. Rational material design for ultrafast rechargeable lithium-ion batteries. *Chem. Soc. Rev.* **2015**, *44*, 5926−5940.

(24) Yang, J.; Wu, Q.; Yang, X.; He, S.; Khan, J.; Meng, Y.; Zhu, X.; Tong, S.; Wu, M. Chestnut-Like TiO2@ α-Fe2O3 Core−Shell Nanostructures with Abundant Interfaces for Efficient and Ultralong Life Lithium-Ion Storage. *ACS Appl. Mater. Interfaces* **2017**, *9*, 354−361.

(25) Aurbach, D.; Markovsky, B.; Weissman, I.; Levi, E.; Ein-Eli, Y. On the correlation between surface chemistry and performance of graphite negative electrodes for Li ion batteries. *Electrochim. Acta* **1999**, *45*, 67−86.

(26) Zhang, Z.; Yoshikawa, H.; Zhang, Z.; Murayama, T.; Sadakane, M.; Inoue, Y.; Hara, M.; Ueda, W.; Awaga, K. Synthesis of Vanadium−Incorporated, Polyoxometalate−Based Open Frameworks and Their Applications for Cathode−Active Materials. *Eur. J. Inorg. Chem.* **2016**, *8*, 1242−1250.

(27) Nyman, M.; Burns, P. C. A comprehensive comparison of transition-metal and actinyl polyoxometalates. *Chem. Soc. Rev.* **2012**, *41*, 7354−7367.

(28) Ji, Y.; Huang, L.; Hu, J.; Streb, C.; Song, Y. F. Polyoxometalate-functionalized nanocarbon materials for energy conversion, energy storage and sensor systems. *Energy Environ. Sci.* **2015**, *8*, 776−789.

(29) Chen, J. J.; Symes, M. D.; Fan, S. C.; Zheng, M. S.; Miras, H. N.; Dong, Q. F.; Cronin, L. High−Performance Polyoxometalate-Based Cathode Materials for Rechargeable Lithium-Ion Batteries. *Adv. Mater.* **2015**, *27*, 4649−4654.

(30) Xie, J. J.; Zhang, Y.; Han, Y. L.; Li, C. L. High-Capacity Molecular Scale Conversion Anode Enabled by Hybridizing Cluster-Type Framework of High Loading with Amino-Functionalized Graphene. *ACS Nano* **2016**, *10*, 5304−5313.

(31) Kawasaki, N.; Wang, H.; Nakanishi, R.; Hamanaka, S.; Kitaura, R.; Shinohara, H.; Yokoyama, T.; Yoshikawa, H.; Awaga, K. Nanohybridization of polyoxometalate clusters and single-wall carbon nanotubes: applications in molecular cluster batteries. *Angew. Chem., Int. Ed.* **2011**, *50*, 3471−3536.

(32) Nishimoto, Y.; Yokogawa, D.; Yoshikawa, H.; Awaga, K.; Irle, S. Super-reduced polyoxometalates: excellent molecular cluster battery components and semipermeable molecular capacitors. *J. Am. Chem. Soc.* **2014**, *136*, 9042−9052.

(33) Ma, D.; Liang, L.; Chen, W.; Liu, H.; Song, Y. F. covalently Tethered Polyoxometalate−Pyrene Hybrids for Noncovalent Sidewall Functionalization of Single-Walled Carbon Nanotubes as High-Performance Anode Material. *Adv. Funct. Mater.* **2013**, *23*, 6100−6105.

(34) Wang, Y. Y.; Zhang, M.; Li, S. L.; Zhang, S. R.; Xie, W.; Qin, J. S.; Su, Z. M.; Lan, Y. Q. Diamondoid-structured polymolybdate-based metal-organic frameworks as high-capacity anodes for lithium-ion batteries. *Chem. Commun.* **2017**, *53*, 5204−5207.

(35) Zhu, P. P.; Sheng, N.; Li, M. T.; Li, J. S.; Liu, G. D.; Yang, X. Y.; Jiang, J.; Sha, J.-Q.; Zhu, M.-L. Fabrication and electrochemical performance of unprecedented POM-based metal−carbene frame-works. *J. Mater. Chem. A* **2017**, *5*, 17920−17925.

(36) Sha, J.; Zhu, P.; Yang, X.; Li, X.; Li, X.; Yue, M.; Zhou, K. Polyoxometalates Templated Metal Ag−Carbene Frameworks Anodic

Material for Lithium-Ion Batteries. *Inorg. Chem.* **2017**, *56*, 11998−12002.

(37) Sheldrick, G. M. *SHELX-97, Program for Crystal Structure Refinement*; University of Göttingen: Göttingen, Germany, 1997.

(38) Evans, H. T., Jr; Popev, M. T. Reinterpretation of five recent crystal structures of heteropoly and isopoly complexes: divanadodecamolybdophosphate, trivanadoenneamolybdophosphate, "gamma.-dodecatungstophosphate", the dodecamolybdate-dodecamolybdomolybdate blue complex, and dihydrogen decavanadate. *Inorg. Chem.* **1984**, *23*, 501−504.

(39) Bondi, A. J. van der Waals volumes and radii. *J. Phys. Chem.* **1964**, *68*, 441−451.

(40) Fong, R.; Sacken, U.; Dahn, J. R. Studies of Lithium Intercalation into Carbons Using Nonaqueous Electrochemical Cells. *J. Electrochem. Soc.* **1990**, *137*, 2009−2013.

(41) Wei, T.; Zhang, M.; Wu, P.; Tang, Y.-J.; Li, S.-L.; Shen, F.-C.; Wang, X.-L.; Zhou, X.-P.; Lan, Y.-Q. POM-based metal-organic framework/reduced graphene oxide nanocomposites with hybrid behavior of battery-supercapacitor for superior lithium storage. *Nano Energy* **2017**, *34*, 205−214.

(42) Li, M. T.; Cong, L.; Zhao, J.; Zheng, T. T.; Tian, R.; Sha, J. Q.; Su, Z. M.; Wang, X. L. Self-Organization towards Complex Multi-Fold Meso-Helixes in the Structures of Wells-Dawson Polyoxometalate Based Hybrid Materials for Lithium-Ion Batteries. *J. Mater. Chem. A* **2017**, *5*, 3371−3376.